Chapter 5

The Counterrotating Core and Nuclear Black Hole in IC 1459[1]

Abstract

The E3 giant elliptical galaxy IC 1459 is the prototype galaxy with a fast counterrotating stellar core. For this object we have obtained high S/N long-slit CTIO spectra, from which also the higher order Gauss-Hermite (GH) moments (h_3–h_6) could be reliably extracted, along five position angles. Here we present results based on fully general self-consistent three-integral axisymmetric models of the stellar kinematics, obtained with Schwarzschild's numerical orbit superposition method. In this Chapter we show that with the available data it is possible to study the internal dynamics of this object and try to find constraints on the formation process of the observed counterrotating component. Our modeling results suggest that the kinematically decoupled component is constituted by stars that appear well separated from the rest of the galaxy in integral space. In particular our study indicates that the stars in this component counterrotate along orbits that are close to circular. We are able to estimate the mass involved to be $\approx 1\%$ of the total galaxy mass or $\approx 3 \times 10^9$ $M_\odot$. This value is close to the mass of the Black Hole (BH) that we measure in the nucleus of this object. These results are consistent with the idea that the stellar disk formed from an externally acquired gaseous component, which settled in a thin disk and subsequently turned into star. The acquired material could also have provided the material for the BH growth.

5.1 Introduction

The E3 giant elliptical galaxy IC 1459 ($M_V = -21.19$, $D = 16.5/h$ Mpc, Faber et al. 1989), is a member of a loose group composed mainly of spirals. It shows clear signs of past interaction as evidenced by stellar "spiral arms" detected on deep photographs (Malin 1985), and shells at large radii (Forbes & Reitzel 1995). In its nuclear regions it has a fast counterrotating stellar core, first reported by Franx & Illingworth (1988). This does not stand out as a separate component in HST photometric observations. A blue LINER source (unresolved at HST resolution), surrounded by patchy dust absorption and by a gaseous disk, is found at its very center (Verdoes Kleijn 2000; Carollo et al. 1997; Forbes et al. 1995).

[1]Cappellari, M., Verolme, E.K., van der Marel, R.P., Verdoes Kleijn, G.A., Franx, M., Carollo, C.M., de Zeeuw, P.T. 2000, in preparation

The kinematics of the nuclear gaseous disk, as determined from Hubble Space Telescope (HST) Faint Object Spectrograph observations in combination with WFPC2 photometry, has been analyzed by Verdoes Kleijn et al. (2000) to measure the mass of the supermassive Black Hole (BH) in this galaxy, which resulted in $M_\bullet = 1 - 4 \times 10^8$ M$_\odot$. Isotropic dynamical models for the major axis stellar kinematics were also produced.

In this Chapter we use an axisymmetric three-integral orbit-superposition Schwarzschild's method (Rix et al. 1997; van der Marel et al. 1998; Cretton et al. 1999) to model deep, ground-based spectroscopic observations, along five slit positions. We show that in this way it is possible to derive information on the nature of the kinematically decoupled nuclear component, and provide useful constraints on its formation process. We also provide an independent mass determination for the nuclear BH in this galaxy.

Throughout this Chapter we assume $h = 0.8$ as in Verdoes Kleijn et al. (2000), although a probably more accurate distance for this galaxy has been recently published by Tonry et al. (2000). This does not influence our conclusions but sets the scale of our models in physical units. Specifically, distances, length and masses scale as h^{-1}, while mass-to-light ratios scale as h.

5.2 Data

5.2.1 Ground-based Spectroscopy

In this chapter we analyze a set of ground-based spectroscopic observations taken with the CTIO 4m telescope in November 1988. These observations were made along five different slit positions with a $1\farcs5$ wide slit, using a CCD with a $0\farcs73$ pixel size. The seeing PSF was $\approx 1\farcs5$ FWHM during the observations. The major axis, two $\pm 45°$ intermediate axes and two positions close to the minor axis were observed. The precise location of the different slit positions is shown in Figure 5.1. The major axis data were presented previously in van der Marel & Franx (1993).

5.2.2 Correction of Patchy Dust Absorption

We intend to derive an I-band surface density model from the available WFPC2/F814W (460 s) Hubble Space Telescope image of IC 1459. This galaxy however contains gas and dust in its central regions and this has to be corrected to obtain an accurate determination of the central stellar surface brightness. We derive the correction, making use also of the available WFPC2/F555W (1000 s) frame, in the same spirit of Carollo et al. (1997), namely by assuming that:

- the galaxy pixels affected by dust have the same intrinsic color as their surrounding regions;
- the dust is a screen in front of the stellar emission;
- the Galactic extinction law (Cardelli, Clayton, & Mathis 1989) applies.

In practice, Carollo et al. (1997) corrected the pixel values by assuming that all the pixels on one isophote have the same intrinsic color. Here we make this correction slightly more robust and more easy to use, in particular in the central regions, by adding the assumption

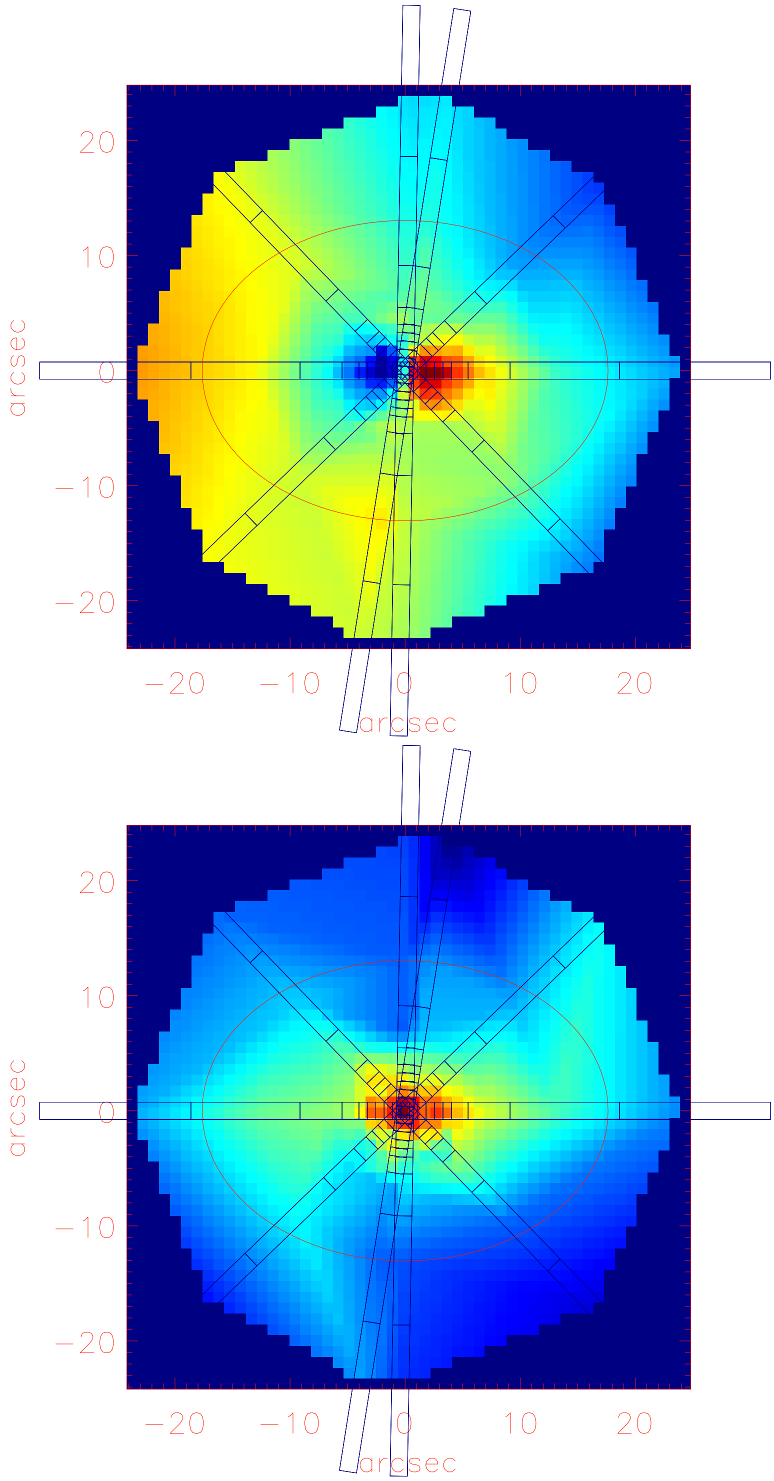

Figure 5.1: IC 1459 observed kinematics. *Upper Panel:* mean velocity field obtained by linear interpolation from the measured values at the aperture positions. The central counterrotating component is clearly visible. A representative galaxy isophote, the five slit positions and the regions along the slits that have been averaged are also shown. *Lower Panel:* same as in the upper panel for the observed velocity dispersion field.

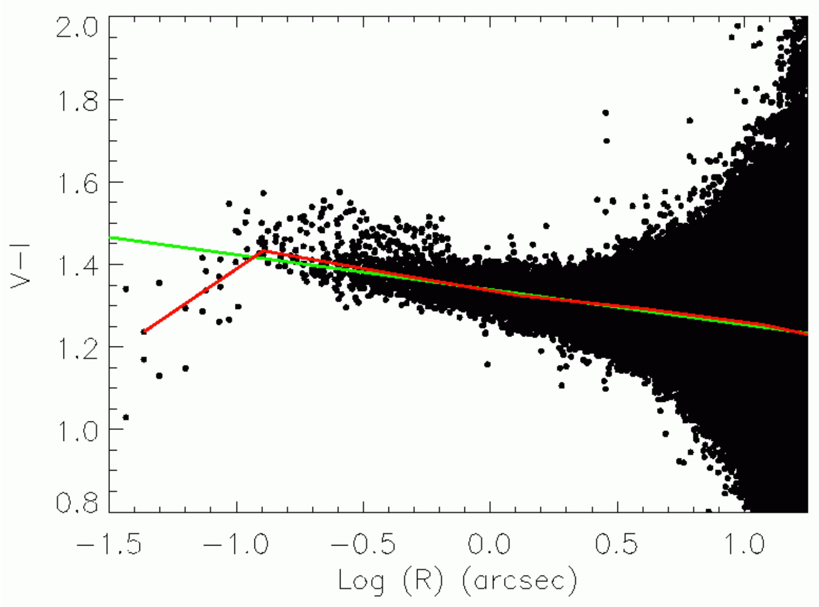

Figure 5.2: The calibrated $V - I$ color of every pixel in the WFPC2/PC1 image of IC 1459, is plotted as a function of its elliptical radius. The best fitting straight line, obtained by minimizing the absolute deviation, is shown as a green line. For comparison, we have plotted with a red line the median color in logarithmically spaced radial bins. Notice the sharp decrease of the color in the nucleus $R < 0''.1$, due to a blue source already detected by Forbes et al. (1995).

that the intrinsic galaxy color also vary smoothly along the radius (e.g. can be parametrized by a power-law or by a spline function). The method goes as follows:

1. we measure the average ellipticity and position angle from the original galaxy image;
2. we construct a calibrated color map (in our case $V - I$);
3. we perform a robust fit with a straight line to the pixel colors as a function of its $\log m$, where m represents the elliptical radius (see Figure 5.2). The fit is done by minimizing the absolute deviation to reduce the effect of large systematic pixel value deviations due to dust;
4. we compute an $E(V - I)$ map by subtracting from all pixels the corresponding color predicted from the previously fitted relation (see Figure 5.3);
5. we correct the pixels, above a given $E(V - I)$ threshold (in general as a function of m), using the standard Galactic extinction curve.

Without entering into the details of the physical significance of this correction we have verified that it is able to correct the major effects of patchy dust absorptions and that it can also be used to measure quick, dust corrected, color gradients (compare Figure 5.2 with Figure 1o in Carollo et al. 1997).

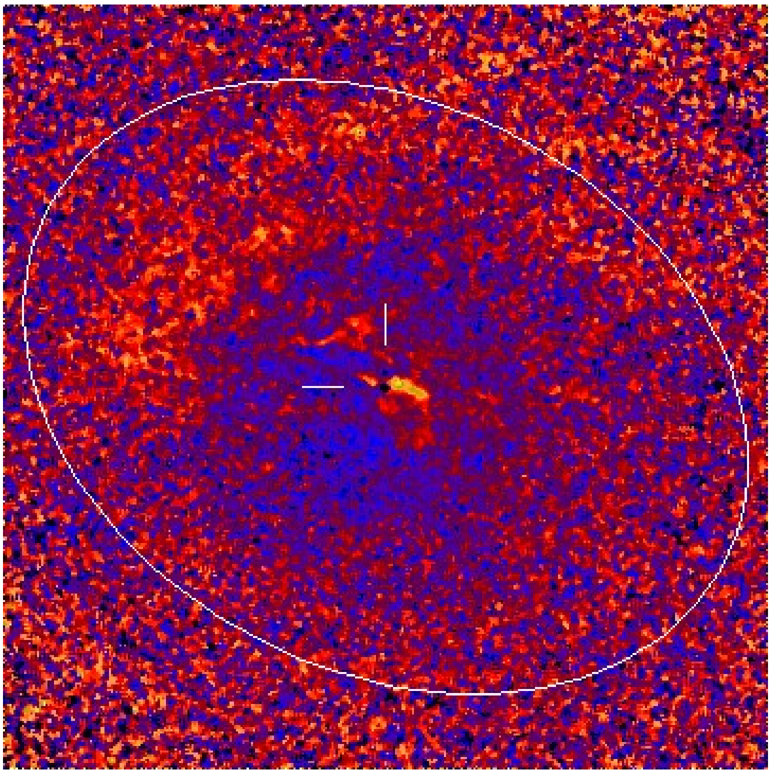

Figure 5.3: $E(V-I)$ map for the central regions of IC 1459, obtained as described in the text after subtraction of the underlying stellar color gradient. Bright colors correspond to larger color excess. Notice the blue central spike (indicated by the two lines) surrounded by heavy dust absorption. A representative galaxy isophote, with an $8''$ semi-major axis, is also shown.

5.2.3 The Mass Model with MGE

IC1459 is not a perfect axisymmetric body, as evidenced by a small $\approx 5^\circ$ isophotal major axis twist in the range $15''$–$100''$ (Franx et al. 1989, Carollo et al. 1997). Nevertheless, the axisymmetric assumption seems reasonable to study its nuclear dynamics.

The first step in the dynamical modeling consists in the determination of a parametrization for the galaxy stellar surface density. For this work we have extended the van der Marel et al. (1998) implementation of the axisymmetric Schwarzschild modeling to use a Multi-Gaussian Expansion (MGE) parametrization for the surface density (Monnet et al. 1992; Emsellem et al. 1994), which also allows for non elliptical isophotes and radial ellipticity variations.

We have obtained an MGE fit to the WFPC2/F814W dust-corrected images of IC 1459 using the fitting algorithm we describe in Chapter 6. A data-model comparison of the MGE fit along seven sectors is shown in Figure 5.4, while the corresponding numerical values of the deconvolved MGE parametrization of the surface density are given in Table 5.1. The central Gaussian represents the contribution of the blue unresolved central spike. Since the axial ratio of this component is not well constrained by the data, due to the undersampling of the WFPC2 PSF, we have set its axial ratio to $q'=1$. It will not be included in the dynamical modeling (because it is probably nonthermal emission), but similar results have also been obtained with all the 11 components. The MGE fit was performed using both the PC1 (at

Table 5.1: MGE parameters for the IC 1459 deconvolved I-band WFPC2 surface brightness

j	P'_j ($L_\odot pc^{-2}$)	σ_j (arcsec)	q'_j
1	791305.8	0.018	1.000
2	17071.9	0.241	0.850
3	22897.4	0.597	0.725
4	11287.8	1.103	0.773
5	10331.5	2.196	0.699
6	5261.6	4.086	0.770
7	1767.2	8.696	0.733
8	543.0	16.69	0.714
9	196.5	28.966	0.795
10	107.0	47.152	0.661
11	58.5	114.688	0.838

full resolution) and WF mosaic together, and the resulting comparison between the isophotes of the convolved model and of the actual image are shown in Figure 5.5. We confirm the finding of Carollo et al. (1997) that there is no photometric evidence for a nuclear disk in the dust corrected images.

5.3 Dynamical Model

5.3.1 Three-Integral Models

In this Chapter we use the most general form of dynamical model available for axisymmetric galaxies, namely the extension of Schwarzschild's (1979) three-integral orbit superposition method which has been developed by Rix et al. (1997), van der Marel et al. (1998) and Cretton et al. (1999). In particular we have adopted the software implementation by van der Marel (vdM) and have adapted it to work with the more general surface density parametrization of the MGE (Monnet et al. 1992, Emsellem et al. 1994). The differences in the code used in this Chapter, compared to the vdM implementation, are:

- elimination of interpolation in the potential and accelerations calculations, that were often required throughout the code. This was made possible by the greater speed in the potential calculation from the MGE parametrization of the surface density (see paragraph 5.3.2);

- elimination of integration of the luminosity density along the line of sight. This was substituted with the analytic deprojection described in the Appendix;

- simplified and more accurate evaluation of the density integration on a polar or Cartesian grid as described in the Appendix.

The method has been extensively described in the above references and we will not repeat the explanation in this Thesis. Very briefly, the method consists in the numerical integration of stellar orbits in the combined axisymmetric potential generated by the stellar density and a central supermassive BH. The stellar density is derived here by deprojecting the observed

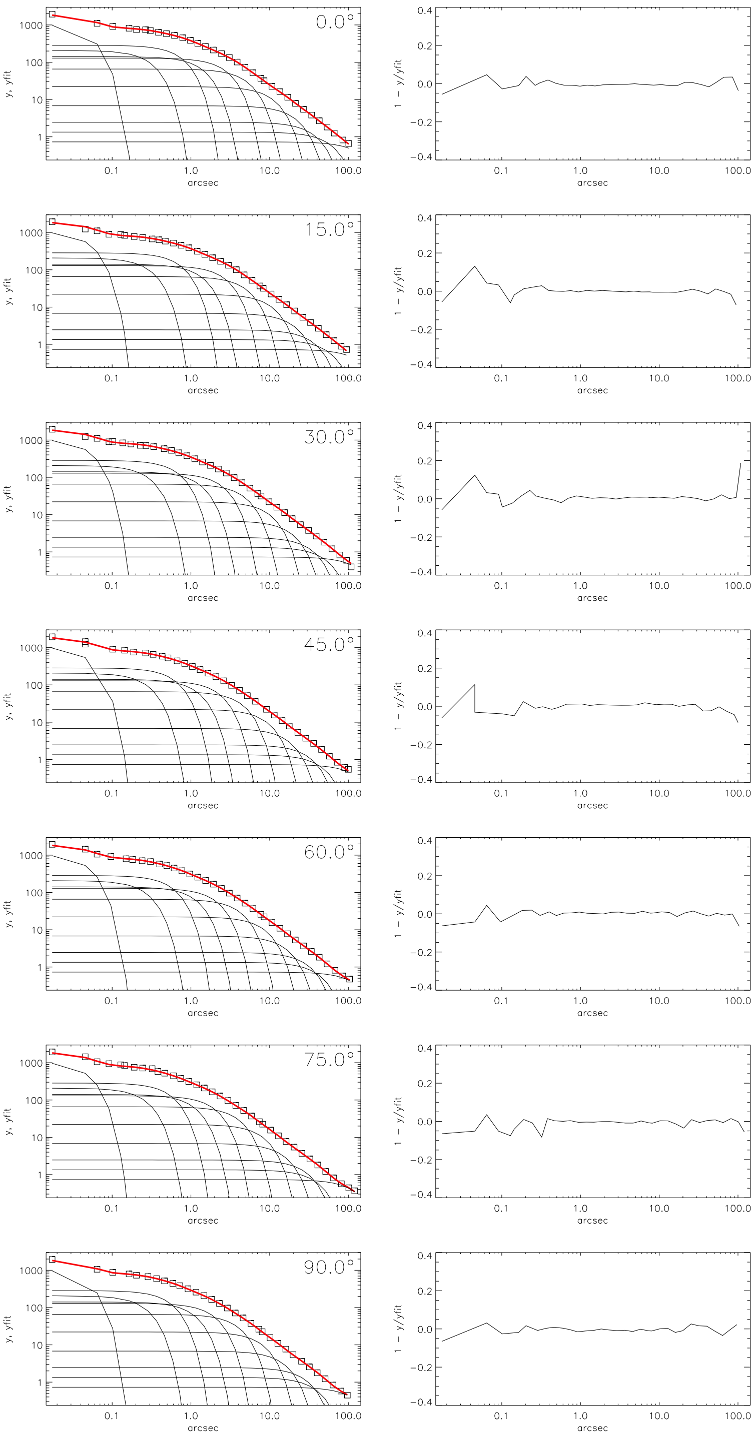

Figure 5.4: *Left Panels:* Comparison between the WFPC2/F814W photometry of IC 1459 and the corresponding MGE best fit model. From top to bottom the profiles are measured along 5° wide sectors, linearly spaced in radius between the major and minor axis. *Right Panels:* radial variation of the relative error along the profiles. Apart from the very innermost pixels where statistical fluctuation are important, the profiles are generally reproduced at the ≈ 1% level in the central range. The RMS error is 0.02 mag.

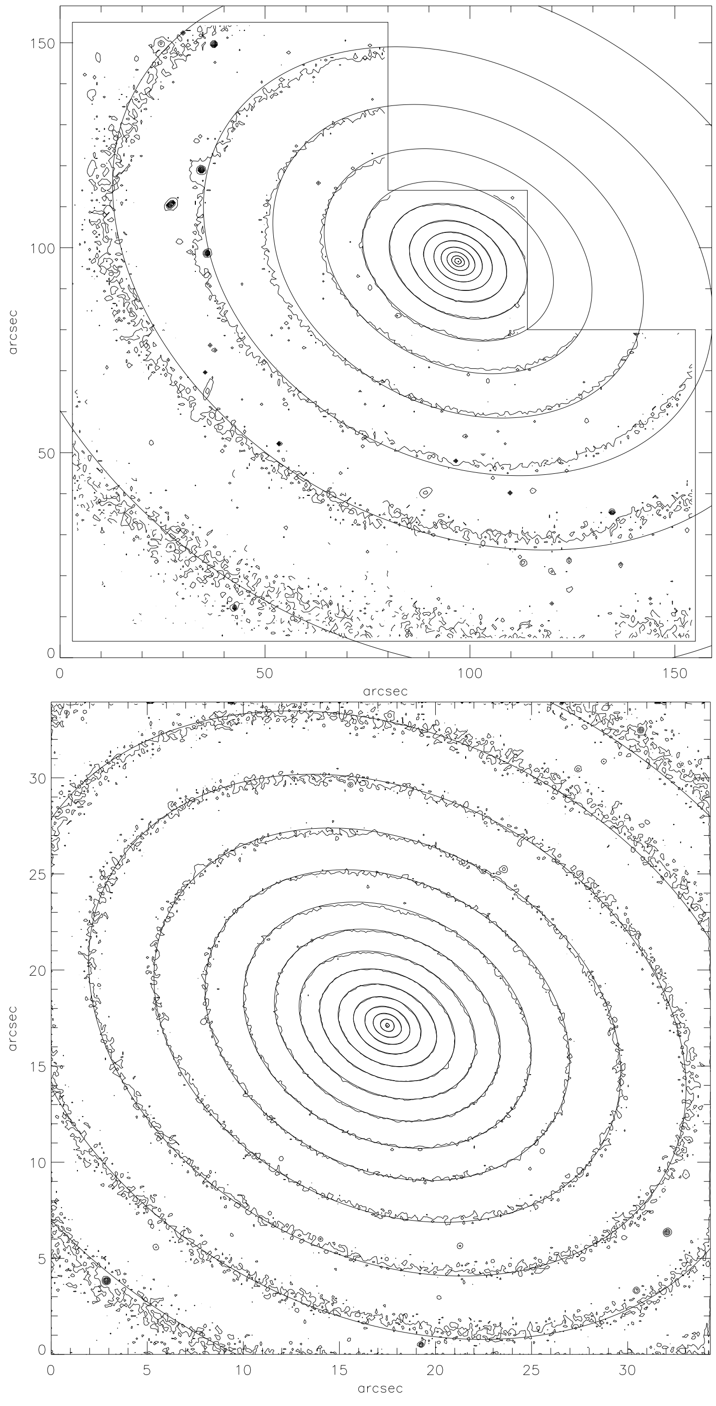

Figure 5.5: Contour maps of the dust-corrected WFPC2 I-band image of IC 1459 at two different scales. *Top Panel:* the whole $160'' \times 160''$ WFPC2 mosaic is shown. *Bottom Panel:* the $35'' \times 35''$ PC1 CCD is presented. Superposed on the two plots are the contours of the intrinsic MGE surface brightness model, convolved with the WFPC2 PSF.

surface density under the assumption of axisymmetry and constant stellar M/L, and adopting the MGE parametrization[1]. Each orbit is then projected onto the space of the observables, taking convolution with the PSF and integration within the apertures into account. Finally a Non-Negative Least-Squares (NNLS) problem is solved to determine the distribution of orbit weights that best fit the observed kinematics, while also reproducing the luminosity density distribution of the model.

Each regular orbit in an axisymmetric potential conserves the energy E, due to the invariance of the system for the choice of the time zeropoint, and the angular momentum L_z along the z axis, due to the invariance for the choice of the angular zeropoint. It also conserves a third non classical integral I_3, which in general is not known analytically (e.g. Binney & Tremaine 1987). To include in the orbit library a representative set of orbits we sample them on a grid covering the full extent of the integral space (E, L_z, I_3).

After some testing we adopted a $20 \times 14 \times 7$ grid in integral space (including both positive and negative L_z), but similar results (with longer computation time) were obtained with a $25 \times 26 \times 13$ grid. The quantity $\eta \equiv L_z/L_{\rm max}$ was sampled linearly on an open grid in the interval $[0, 1]$. The integral I_3 was sampled linearly in the angle w, on an open grid in the interval $[0, w_{\rm th}]$, where $w_{\rm th}$ is the angle w for the "thin tube" orbit at the given (E, L_z) (see Figure 5 in van der Marel et al. (1998) for details). The energy grid was sampled logarithmically in the radius of the circular orbits with the given energy $E(R_c)$, from $0\farcs1$ to $300''$. The adopted radial grid includes 99% of the total galaxy mass.

5.3.2 Potential Calculation

We discuss in this section the techniques that we have adopted to efficiently evaluate the MGE potential during the determination of the orbital starting conditions and during the orbital integration, without the need to interpolate the potential on a grid.

In the following we will always refer to *axisymmetric* MGE models. From the surface density given in Table 5.1, we have analytically derived the deprojected intrinsic density under the MGE assumptions (see Appendix)

$$\rho(R, z) = \sum_{j=1}^{N} P_j \exp\left[-\frac{1}{2\sigma_j^2}\left(R^2 + \frac{z^2}{q_j^2}\right)\right], \tag{5.1}$$

where N is the number of Gaussians adopted in the expansion, P_j are the Gaussian central densities, σ_j are the corresponding dispersions and q_j the intrinsic axial ratios.

The general form for the potential computation with MGE, as obtained using the classic formula for the potential of ellipsoidal bodies (e.g. Chandrasekhar 1969), is given by equations (39,40) in Emsellem et al. (1994)

$$\Psi(R, z) = -4\,\pi\,G \sum_{j=1}^{N} \sigma_j^2\, q_j\, P_j\, \mathcal{Q}_j(R, z), \tag{5.2}$$

with

$$\mathcal{Q}_j(R, z) = \int_0^1 \frac{\exp\left\{-\frac{T^2}{2\sigma_j^2}\left[R^2 + \frac{z^2}{1-(1-q_j^2)T^2}\right]\right\}}{\sqrt{1-(1-q_j^2)T^2}} \cdot dT \tag{5.3}$$

[1]The axisymmetric assumption alone is not sufficient to define a unique deprojection of the surface density.

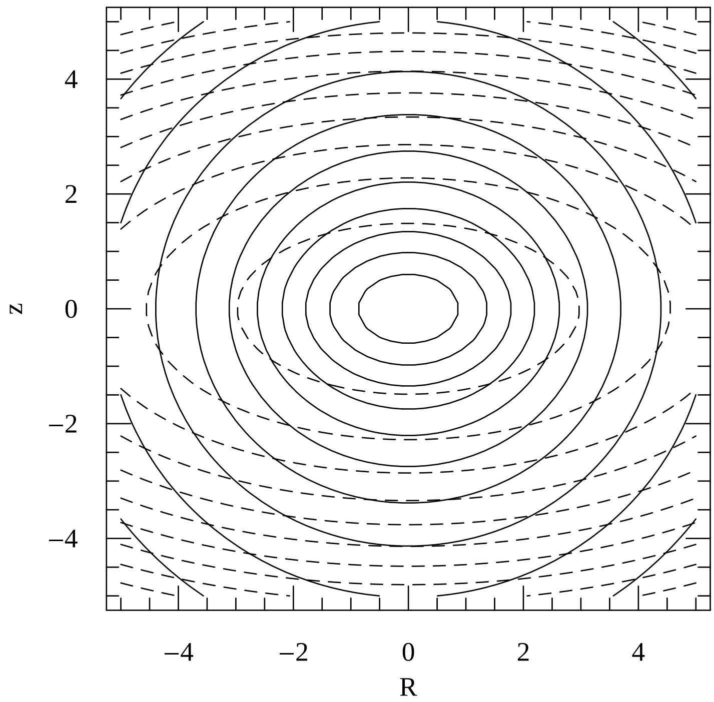

Figure 5.6: The contours of the potential in the meridional plane of a flattened axisymmetric Gaussian (solid lines) are compared to the contours of the corresponding density (dashed lines). Both contours are logarithmically spaced and the axis scale is in unit of σ.

Since the Gaussians of an MGE parametrization are generally logarithmically spaced in σ_j (see Chapter 6), and sample many orders of magnitude in radius, we want to see whether it is necessary to do the actual integration in equation (5.3) or whether instead a limiting expression can be used in real calculations (e.g. during orbit integrations).

It is well known that the contours of the potential of an object, with a density increasing towards the center, are rounder than the contours of the corresponding density. This can be understood from the fact that well outside a sphere that contains essentially all the mass, the density resembles that of a point-like object and the potential looks spherical. In particular, the integrated mass $M(R)$ of a Gaussian within a given radius converges very quickly and the potential consequently becomes spherical very rapidly. An example of this phenomenon in the case of a single Gaussian is shown in Figure 5.6.

To quantify this we show in Figure 5.7, as a function of the axial ratio q, the maximum relative difference between a Gaussian potential and a spherical potential generated by a point mass with the same total mass, along the z and R axis. The maximum difference, for a given distance from the origin, is obtained on the z axis. This plot demonstrates that when $100\,\sigma_j \lesssim (R^2+z^2)$, we can substitute the term $\mathcal{Q}_j(R,z)$ in equation 5.2 with its limiting expression for large radii

$$\mathcal{Q}_j(R,z) = \frac{\sqrt{\pi/2}\,\sigma_j}{\sqrt{R^2+z^2}} \tag{5.4}$$

committing a maximum relative error $\epsilon \lesssim 1\times10^{-4}$. This is a conservative estimate for the total relative error in the potential, since it applies only to one Gaussian, while in practice not all Gaussians in the expansion will be in the most unfavorable condition at the same time.

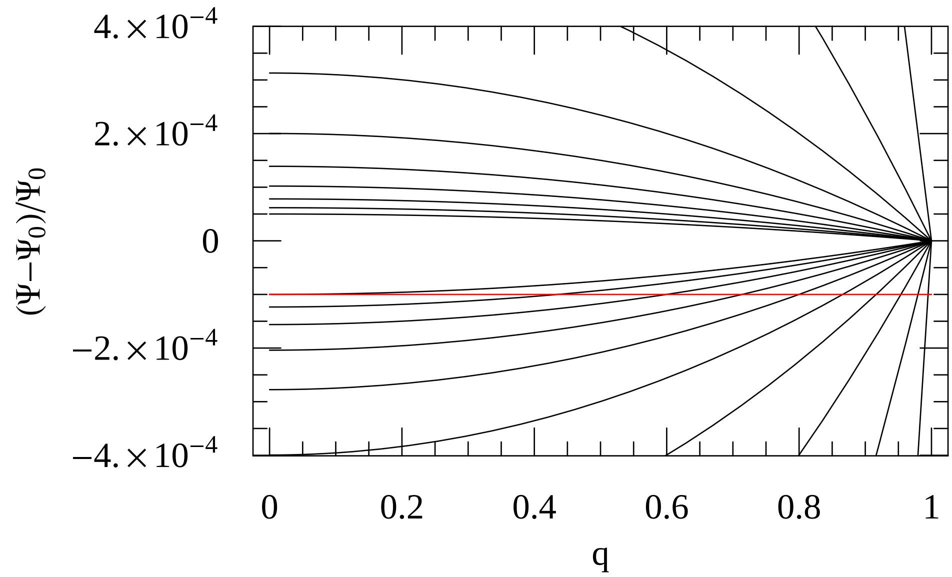

Figure 5.7: The maximum relative difference of a Gaussian potential Ψ from a spherical potential Ψ_0 generated by a point mass with the same total mass, is plotted as function of the intrinsic axial ratio q. The different lines are measured along the symmetry axis, with $z/\sigma = 10, 20, \ldots, 100$ (negative lines) and on the equatorial plane with $R/\sigma = 10, 20, \ldots, 100$ (positive lines). The horizontal line indicates a relative difference of $\epsilon = -1 \times 10^{-4}$.

At the other extreme, a similar reasoning applies in the limit of small radii. In this regime the potential tends to a finite $\Psi(0,0)$ value and we may be able to substitute $\mathcal{Q}_j(R,z)$ with its central analytic value

$$\mathcal{Q}_j(0,0) = \frac{\arcsin\left(\sqrt{1-q_j^2}\right)}{\sqrt{1-q_j^2}} \tag{5.5}$$

if the difference is small enough. In Figure 5.8 we plot the relative difference of a Gaussian potential $\Psi(0,z)$ from its central value $\Psi(0,0)$, as function of the intrinsic axial ratio q. The different lines refer to different distances along the z axis. Assuming a reasonable lower limit on the axial ratio $0.1 < q$ we see from the plot that, if a maximum relative error $\epsilon \lesssim 1 \times 10^{-4}$ is tolerated, we can safely substitute the potential with its central value when $z \lesssim \sigma_j/170$. Given that the maximum difference is obtained on the z axis we can put a conservative condition $(R^2 + z^2) \lesssim \sigma_j/170$ for the use of equation (5.5).

An example of the usefulness of this approximation is given by the present Schwarzschild modeling. We have adopted a grid of orbits in the radial range $0\farcs1 < R < 300''$, and by comparison with Table 5.1 it appears clear that the approximate formulae described in this section will often be used and only a small number of the integrations will actually need to be performed at most positions. Another related advantage of the above conditions is that the cases where approximate relations are used are precisely those where the integrand is badly behaved and most slow to integrate.

Similar considerations are also valid for the two components of the acceleration in the meridional plane (that are required by the orbit integration), and in many other computations involving the MGE expansion, and the three regimes considered above can still be used.

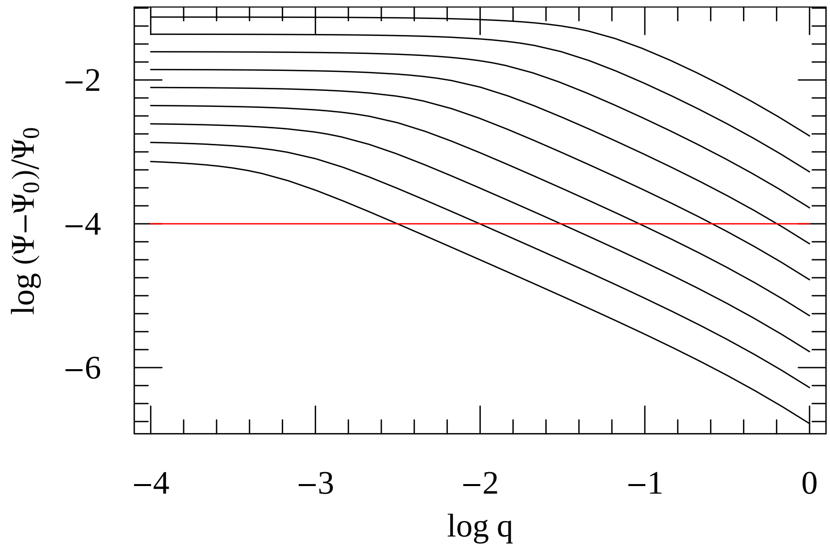

Figure 5.8: The relative difference of a Gaussian potential $\Psi(0,z)$ from its central value $\Psi(0,0)$, is plotted as function of the intrinsic axial ratio q, for $\log(z/\sigma)=-3,-2.75,\ldots,-1$ (from the bottom to the top). The horizontal line indicate a relative error of $\epsilon=1\times10^{-4}$.

Adopting the same radial ranges for the acceleration calculations as for the potential we obtain relative errors that are just slightly larger, $\epsilon\lesssim5\times10^{-4}$ in the worst case (remember that these are worst case values obtained for a single Gaussian with an extreme axial ratio $q=0.1$).

In cases where the integral in equation (5.3) had to be performed, we adopted a globally adaptive, recursive Gauss-Kronrod integration scheme (Favati et al. 1991). The use of a globally adaptive algorithm is very beneficial at low and high distances from the galaxy center (but before the switch to the limiting regimes), where the integrand of equation (5.3) shows a sharp peak close to $T=1$ or to $T=0$ respectively. In these cases the integrand is evaluated more densely only around the peaks.

We finally notice that, while in the axisymmetric case the orbit integration with an MGE potential can be made competitive in speed and more accurate than the interpolation of a precomputed potential on a 2D grid, the use of MGE for the orbit integration in a triaxial body can give large speed gains since the 1D integration that is still required becomes much faster than an interpolation on a 3D grid.

5.3.3 Data-Model Comparison

Our model has three free parameters: the BH mass $M_\bullet$, the stellar mass-to-light ratio Υ and the inclination i. In this Chapter we will not consider the effect of the latter, which is less than the other two parameters, but will keep it fixed to the value $i=60°$, determined in Verdoes Kleijn et al. (2000) from the geometry of an extended gaseous disk that has been observed in IC 1459.

We fitted the dynamical model to the V, σ and h_3–h_6 observations along all five position angles, varying the two free parameters Υ and $M_\bullet$ (Figure 5.9). We obtain $\Upsilon=4.5\pm0.5$ (in the I-band) and $M_\bullet=(2\pm1)\times10^9\ M_\odot$ (adopting $h=0.8$) for the models that provide

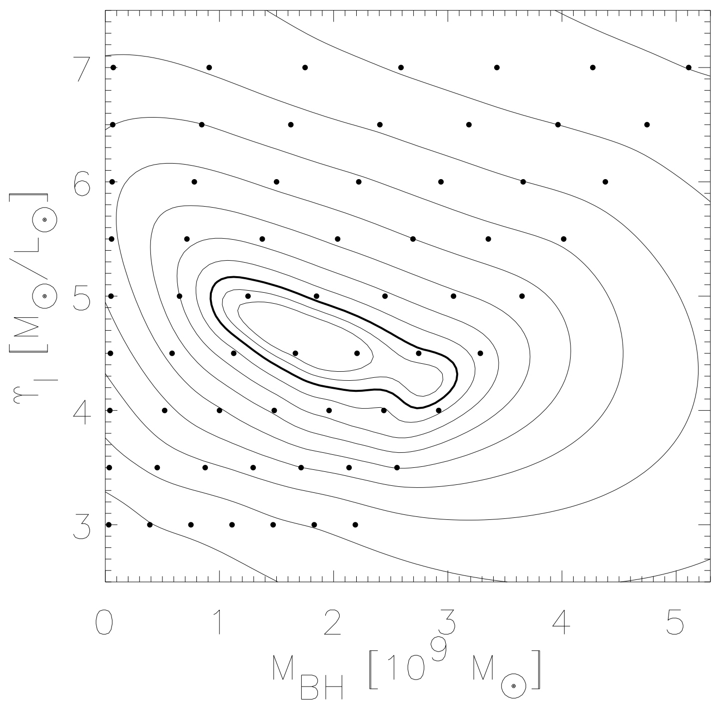

Figure 5.9: Contours of constant χ^2 that measure the goodness of fit of the axisymmetric models to kinematic data for IC 1459. The abscissa is the mass of a central point mass representing a nuclear BH, while the ordinate is the M/L of the stars. These two parameters uniquely determine the potential. For every dot a specific model was constructed using self-consistent three-integral axisymmetric models of the stellar kinematics, obtained with Schwarzschild's numerical orbit superposition method. The contours were obtained through spline interpolation (the first three contours define the formal 68.3%, 95.4%, and [heavy contours] 99.73% confidence regions; subsequent contours are characterized by a factor of 2 increase in $\Delta\chi^2$). The best fit is obtained with a mass for the BH $M_{BH} \simeq 2 \times 10^9 M_\odot$ and a stellar $M/L \simeq 4.5$ in the I-band.

statistically acceptable χ^2 values. The excellent match (Figures 5.10–5.12) to *all* the observed kinematical constraints, along *all* position angles, argues that the decoupled core in IC 1459 can be well described as an axisymmetric component, and will allow us to study its internal dynamics, shape and mass distribution.

The formal best fit $M_\bullet$ derived here is significantly larger than that obtained by Verdoes Kleijn et al. (2000) using HST/FOS observations of the gas kinematics, and also lies slightly above the estimate of $\approx 10^9 M_\odot$ based on the relation between $M_\bullet$ and σ proposed by Ferrarese & Merritt (2000) and Gebhardt et al. (2000). However the high value has to be treated with caution, since our ground-based spectroscopy does not resolve the radius of influence of the BH. We have recently obtained STIS spectroscopy to measure the stellar velocity dispersion closer to the nucleus, and these will be included later in our dynamical models, to obtain a more accurate constraint on the BH mass.

The fits shown in Figures 5.10–5.12 where computed without imposing any other constraints than to fit the photometry and kinematics. In the NNLS fit there are $20\times14\times7 = 1960$ orbits, whose weights are the unknowns that have to be determined. On the constraints side

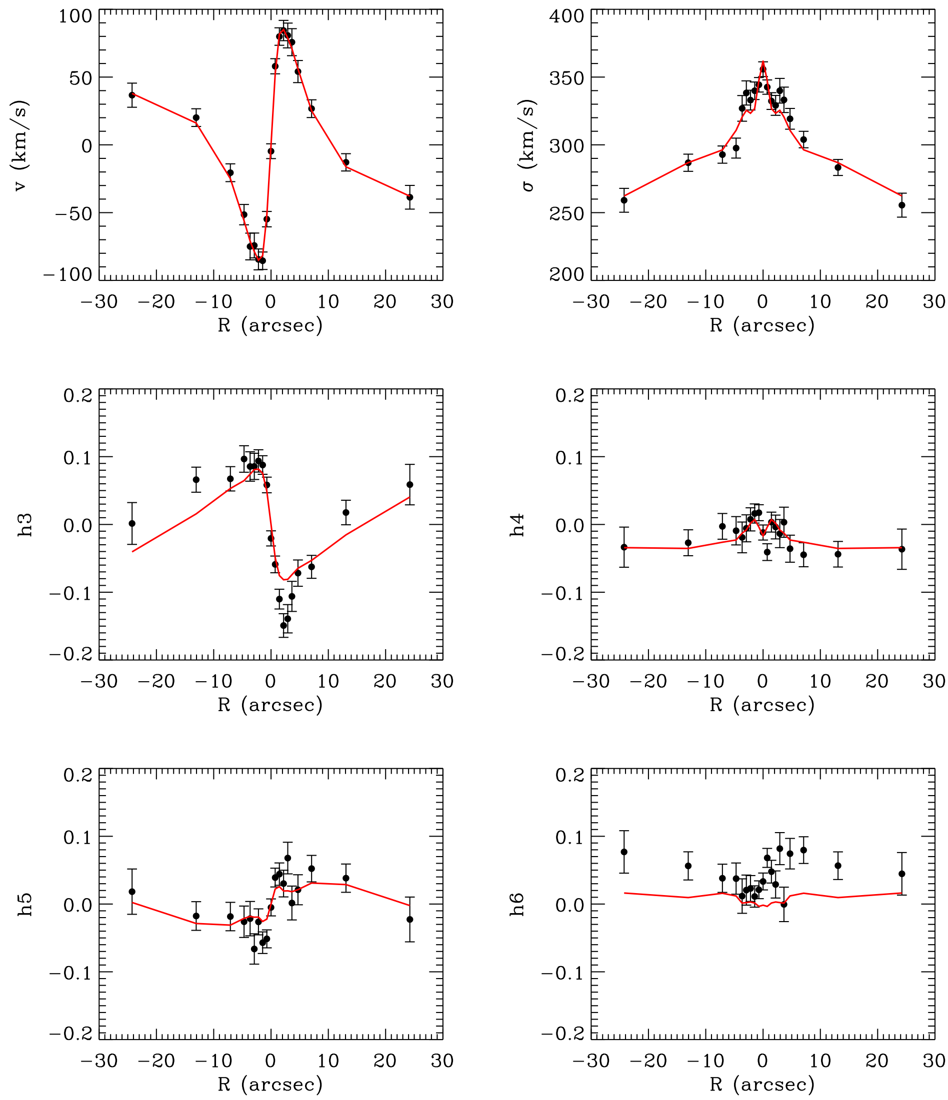

Figure 5.10: Major axis results: the six panels represent respectively, from left to right and from top to bottom, the mean velocity, the velocity dispersion and the higher order Gauss-Hermite moments ($h3 - h6$). The filled circles with error bars represent the measurements, while the solid line gives the prediction of the best fit dynamical model, taking seeing and pixel binning into account.

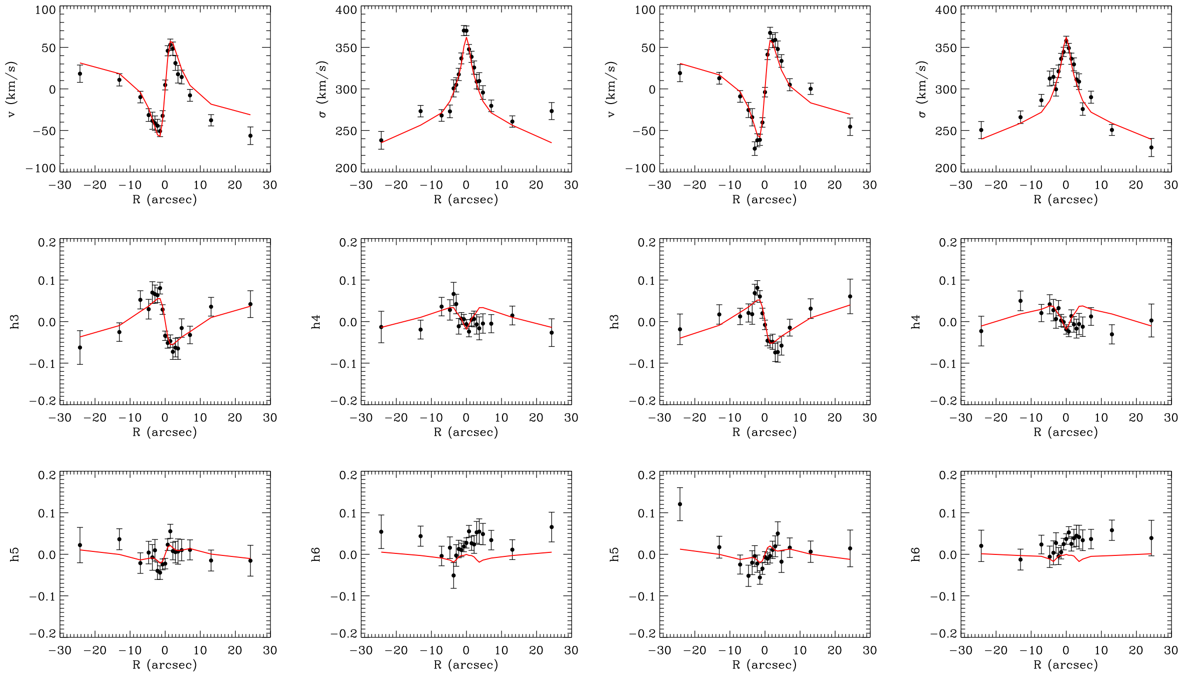

Figure 5.11: Same as figure 5.10 for the two ±45° intermediate axes kinematic observations.

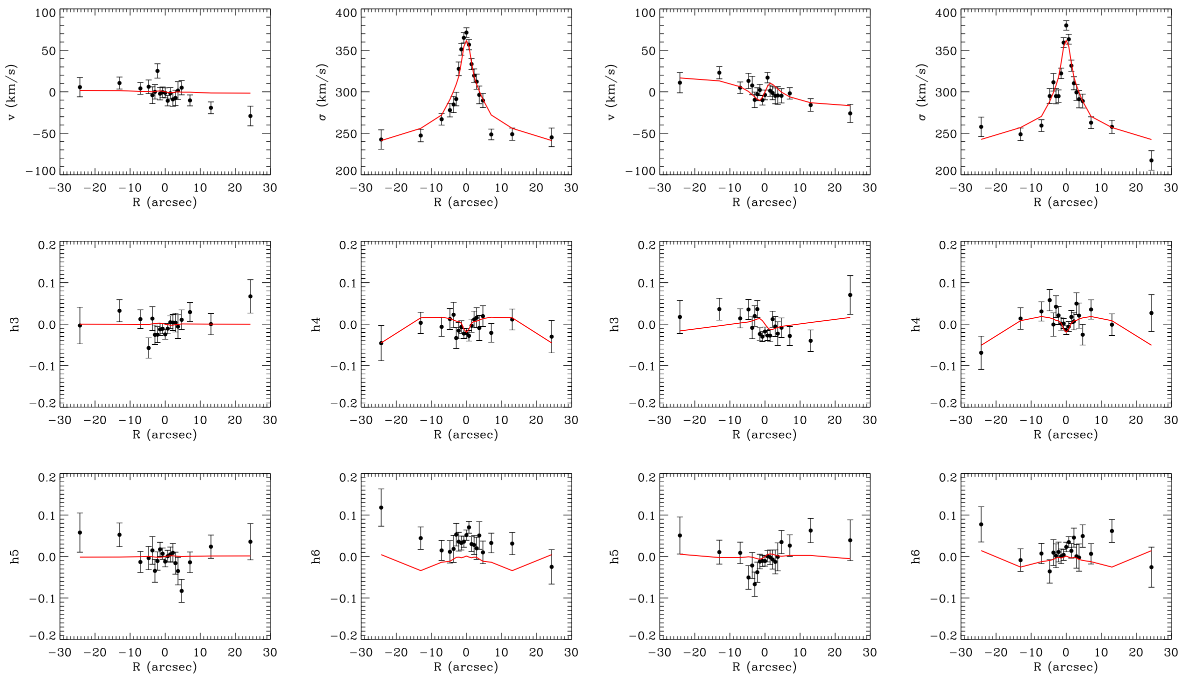

Figure 5.12: Same as figure 5.10 for the two minor axis kinematic observations.

we have 95 kinematical apertures (some not completely independent) with 6 Gauss-Hermite moments determination and the aperture projected mass. We also fit the photometry in the meridional plane (120 constraints) and in the projected plane (another 140 constraints). There are thus 925 constraints in total, not completely uncorrelated, from which one cannot expect to be able to determine a unique combination of 1960 weights that defines the internal dynamics of this galaxy (in the approximation of this model). In fact, the NNLS matrix equation that is solved is numerically rather ill-conditioned, giving rise to a distribution function composed of sharp isolated peaks. Such DFs are unphysical. Smoothing in the solution space can be achieved via regularization. The scheme adopted for this is based on a minimization, up to a certain degree, of the differences in weights between neighboring orbits. Although the extra regularization constraints lead to a poorer fit to the data, a considerable amount of smoothing can be enforced on the solution before the differences in the fit become appreciable.

In Figure 5.13 we show the integral space [the weighs on the (E, L_z, I_3) grid] of the NNLS solution of our modeling of the IC 1459 kinematics, for a selected set of energies (corresponding to the radii effectively constrained by the observations). The top row represents the solution obtained without any smoothing and the integral space looks very noisy. A small regularization ($\Delta = 5$; see van der Marel (1998) for details) was added as a constraint in the middle row. While the fit to the data remains essentially unchanged, the solution space changes abruptly, due to the ill-conditioning of the non-regularized solution, and some structures clearly emerge. The bulk of the galaxy rotation is recognizable as a large bright (high weight) region at low and negative $\eta \equiv L_z/L_{\rm max}$ and high w, from $\approx 2''$ to the last measured point $\approx 25''$. The most interesting fact is the appearance of a well separated region that counterrotates with respect to the main galaxy body and is present at $\eta \approx 1$ (nearly circular orbits). The behavior already described in the middle row becomes more clearly visible at high regularization ($\Delta = 1$) in the bottom row. This latter model is still able to produce a reasonable fit to all constraints, yet the integral space of the solution appears very smooth and regular. The striking exception to this smoothness is the well isolated $\eta \approx 1$ region that is visible in the radial range $1''$–$5''$(panels 2–5). This group of orbits in nearly circular motion appears necessary to explain the observed rapid counterrotation in the kinematics.

Given that the counterrotating component appears so well isolated from the rest of the orbital distribution, it becomes possible to make a quantitative estimate of the mass involved. This is something that was not possible by any other means, due to the fact that the counterrotating component is not apparent from the photometry and does not appear as a double component in the LOSVD. By summing the mass weights in the orbits of the solution contributing to the counterrotation we find that this component constitutes $\approx 1\%$ of the galaxy mass or $\approx 3 \times 10^9$ $M_\odot$, where the total galaxy mass was determined from the Gaussian components of Table 5.1.

In Figure 5.14 we show the V/σ field in the meridional plane of the model. This was computed by summation of the velocity moments of the orbits in the best fitting solution with high regularization of Figure 5.13. The flattened appearance of the counterrotating stellar component is clearly visible from this map.

It was shown by Cretton & van den Bosch (1999) that the Gauss-Hermite (GH) parametrization for the Line-Of-Sight Velocity Distribution (LOSVD), that is used as the kinematical constraints within the present implementation of the Schwarzschild modeling, can in some special cases produce artificial counterrotations. This is essentially due to the fact that the model is trying to reproduce a small number of GH moments and not the actual observed LOSVD, and when two functions coincide on a small set of GH moments this does not guar-

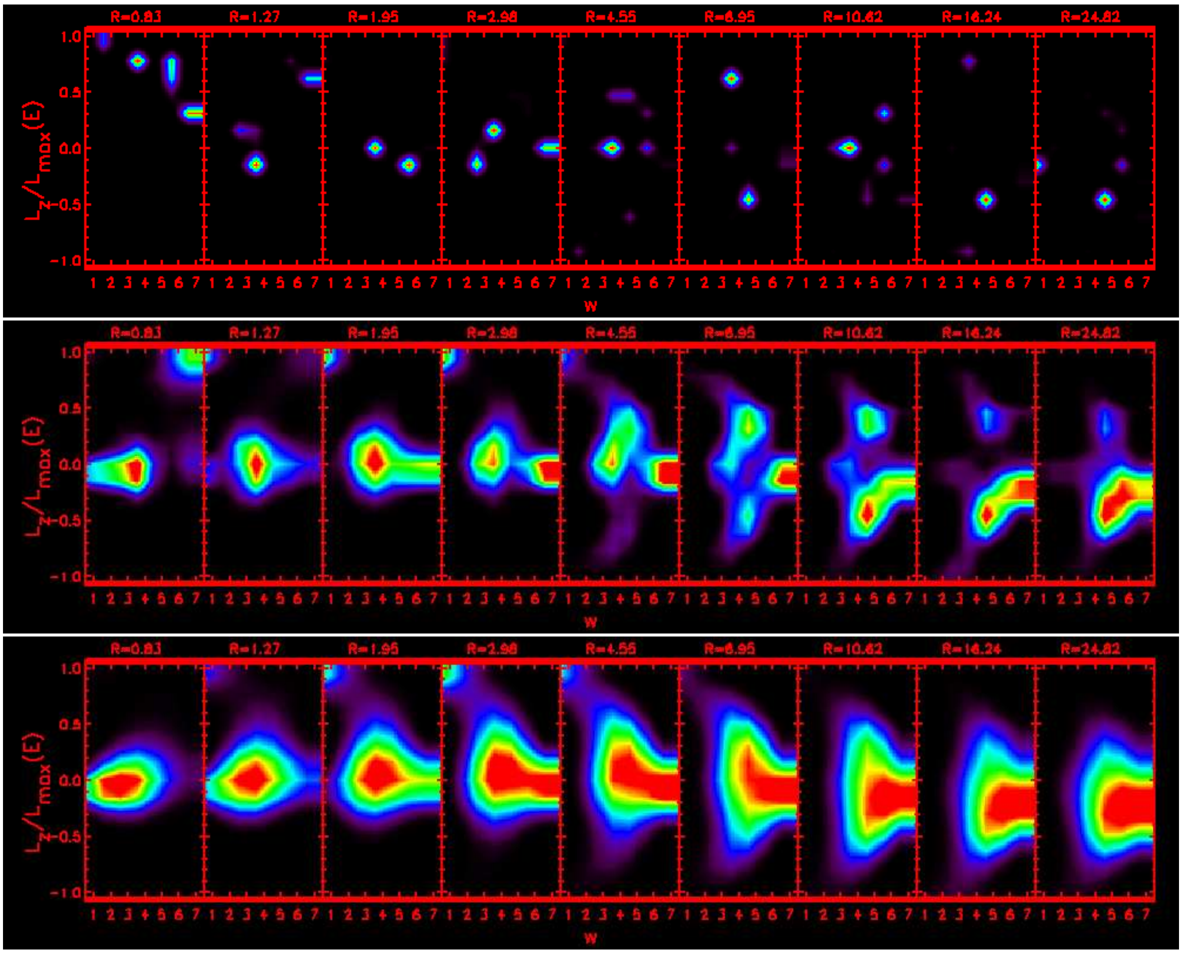

Figure 5.13: The top row shows the (η, w) integral space (defined as described in the text) for a selected set of energies, for the best-fitting non-smooth orbit-superposition model. The radius of the circular orbit (in arcsec) at each given energy is printed at the top of each panel, and only the radii that are actually constrained by the observed data are shown. At each energy the plots have been obtained by linear interpolation from a 14×7 grid in (η, w), where each (η, w) represents an orbit. The colors show the fraction of the mass at the given energy that was assigned to each orbit by the NNLS fit (bright colors correspond to large weights). Smoother solutions are obtained by adding regularization constraints to the NNLS fit. The second and third rows show the integral space for the same model with a modest ($\Delta = 5$) and a large ($\Delta = 1$) amount of regularization, respectively. Negative $\eta \equiv L_z/L_{\max}(E)$ in this plot correspond to the bulk rotation of the galaxy body. The counterrotating component is clearly recognizable as a well separated peak at $\eta \approx 1$ in the central and bottom row, in the radial range $1'' - 5''$ (panels 2−5 from the left).

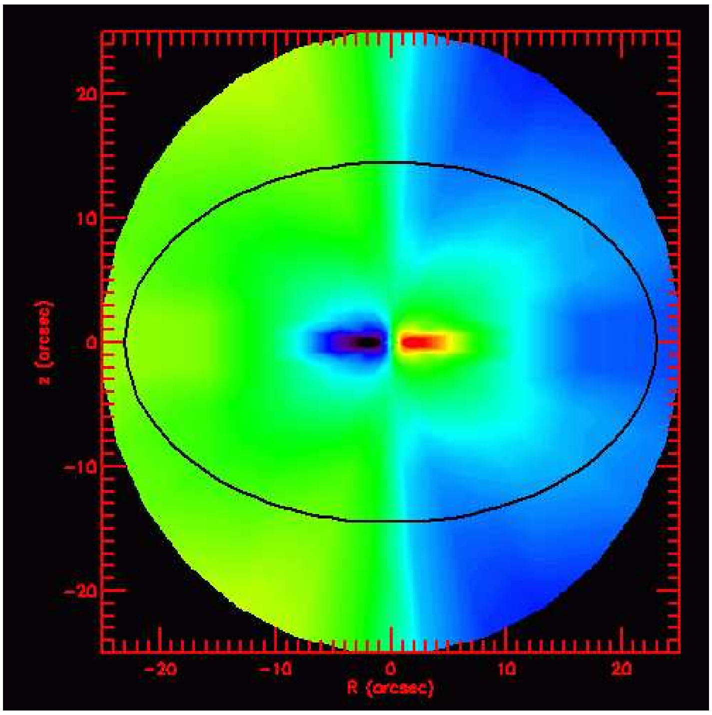

Figure 5.14: The V/σ field, computed from the velocity moments of the best fitting high regularization solution of Figure 5.13. The flattened appearance of the $R < 5''$ counterrotating component is readily apparent from this map. A representative galaxy isodensity contour is also shown. Note that this field was computed from the orbital solution moments on a complete grid in the galaxy meridional plane and was *not* interpolated from the values in a few aperture positions (as done in Figure 5.1).

antee that they are the same function [see Cretton & van den Bosch (1999) for details]. This phenomenon however can be easily recognized after the fit, by comparing the LOSVDs predicted by the model and the observed ones. Before proceeding with the interpretation of the IC 1459 internal dynamics we check that our best fit dynamical model does not suffer from this shortcoming.

To test this we plot in Figure 5.15 a comparison between the LOSVD of the model with high regularization ($\Delta = 1$), obtained by direct summation on the velocity histograms of the best fitting orbits, and the actual measured LOSVD, as determined from the parametrization introduced by van der Marel & Franx (1993)

$$\mathcal{L}(v) = \frac{\gamma}{\sqrt{2\pi}\sigma} e^{-\frac{1}{2}w^2} \left[1 + \sum_{j=3}^{6} h_j H_j(w) \right], \tag{5.6}$$

where

$$w \equiv (v - V)/\sigma. \tag{5.7}$$

Here v is the line-of-sight velocity, H_j are the Hermite polynomials of degree j, which are also tabulated in the Appendix, and h_j are the Gauss-Hermite coefficients which are plotted in Figure 5.10–5.12. It is apparent from this comparison that the model provides an excellent fit

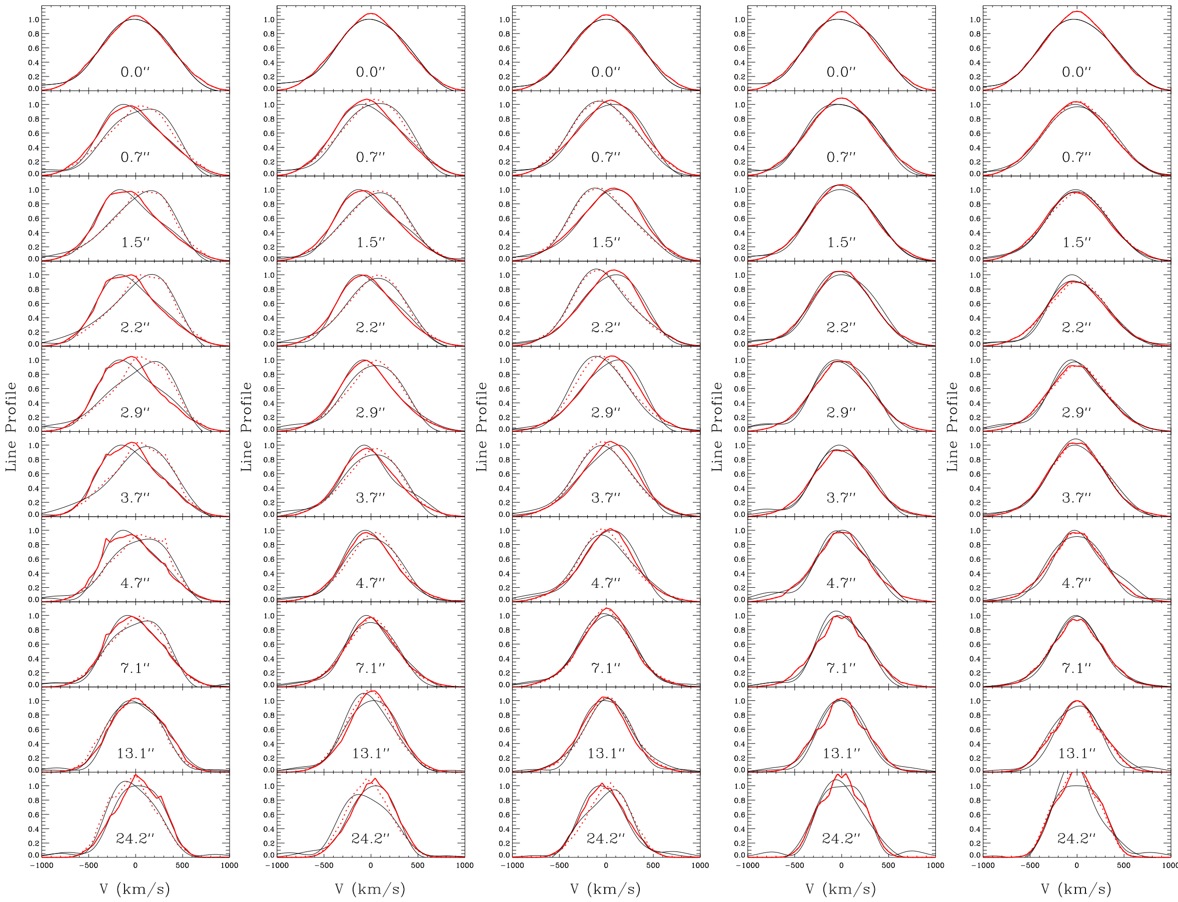

Figure 5.15: The LOSVD predicted by the Schwarzschild modeling with high regularization (thick line: solid and dotted for the two sides of the galaxy respectively) is compared to the observed one, as computed from the first six Gauss-Hermite moments. The columns represent, from left to right, the major axis, the two intermediate and the two minor axes.

to the observed LOSVD, at least well within the errors suggested by the observed differences in the LOSVD at opposite sides of the galaxy. We can thus safely affirm that we are *not* in a situation similar to that shown in Figure 10 of Cretton & van den Bosch (1999) and that our model correctly reproduces the data.

5.4 Discussion and Conclusions

In this chapter we have studied the dynamics of the elliptical galaxy IC 1459 using fully general self-consistent axisymmetric dynamical models based on Schwarzschild's orbit superposition method. The intrinsic density is obtained by deprojecting the observed HST/WFPC2 surface density using an MGE parametrization, after correction for the effects of patchy dust absorption. The axisymmetric model provides an excellent fit to all ground-based kinematical constraints along five slit positions, namely to all Gauss-Hermite moments, while also matching the observed HST photometry. Moreover we have verified that the model velocity histograms actually reproduce the observed LOSVDs and not only its moments.

The good match to the observations obtained with an axisymmetric model provides a test that the counterrotating core in IC 1459 can be accurately described as an axisymmetric stellar component. We have explored the χ^2 map as a function of the two free parameters of the problem $(\Upsilon, M_\bullet)$ and have subsequently analyzed the best fit solution by adding linear regularization constraints in the integral space. The observations can only be reproduced by a regularized model if $\approx 1\%$ of the galaxy stellar mass ($\approx 3 \times 10^9$ $\mathrm{M}_\odot$) counterrotates in the radial range $R \lesssim 5''$ on nearly circular orbits in a flattened disk. This counterrotating component is found to be very well separated from the bulk of the stars in integral space. The mass estimation of the counterrotating stellar component is only made possible by this dynamical modeling, since the decoupled component does not show up in the surface brightness or color maps and cannot be isolated from the observed line profiles. These results can be explained by the following scenario:

- the stellar counterrotating core in IC 1459 has an external origin, as shown by its clear isolation in integral space from the bulk of the stars in the galaxy;
- the core was formed by acquisition of a gas rich component, that settled into a disk in the galaxy potential and later turned into stars. This acquisition must have happened long ago, since the current stellar core also counterrotate with respect to the IC 1459 nuclear gaseous disk (Verdoes Kleijn et al. 2000);
- the fact that the counterrotating core mass is relatively close to the BH mass in this galaxy, as is not uncommon among other stellar disks photometrically determined in other galaxies (Scorza & van den Bosh 1998), leads us to speculate that the IC 1459 counterrotating disk could have been an important accretion source for the BH in the past.

HST/STIS observations have been already obtained by us for this galaxy and they will give stronger constraints on the nuclear BH mass determination, thus also providing further constraints on the nuclear potential and the inferred internal dynamics. We note that IC 1459 is one of the first galaxies for which an independent BH mass determination is being independently attempted using both HST observations of the gaseous kinematics (Verdoes Kleijn et al. 2000) and with fully general three-integrals dynamical models of the stellar kinematics. This will provide a direct test of the accuracy of current BH mass measurements. This is a key factor in the interpretation of the BH mass correlation with other global galaxy parameters and its scatter (e.g. Ferrarese & Merritt 2000, Gebhardt et al. 2000), and consequently of its relation to the galaxy formation process.

With the availability of 2D spectroscopic detectors on large telescopes it will be possible to obtain full 2D distributions of Velocity Profiles, and also line-strength, of kinematically decoupled cores (e.g. Davies et al. 2001). This kind of observations will provide a much larger number of kinematical constraints than what can be obtained from a small number of slit positions, and this is expected to make the dynamical results less dependent on the adopted smoothing. In turn this will improve the robustness of internal dynamical studies such as that presented in this Chapter.

Acknowledgements

It is a pleasure to thank Tim de Zeeuw for his kind hospitality at the Leiden Observatory in the period during which this work was initiated.

5.5 Appendix

5.5.1 MGE Deprojection

The deprojection of a general triaxial galaxy, described with the MGE parametrization has been already discussed in Monnet et al. (1992). We summarize here their results specialized to the axisymmetric case. It is known (Ribicky 1986) that in general the deprojection will not be unique even in the axisymmetric case. The deprojection under the MGE assumptions represents one of the possible solutions to the problem.

Assume that the intrinsic stellar density in the meridional plane (R, z) is given by a sum of 2D Gaussians as in Equation (5.1). Define $m^2 = R^2 + z^2/q^2$ and use, for every single Gaussian component the following equation that is valid for general axisymmetric spheroidal models (e.g. equation (3.2) in Qian et al. (1995))

$$\Sigma(m'^2) = \frac{q}{q'} \int_{m'^2}^{\infty} \frac{\rho(m^2)dm^2}{\sqrt{m^2 - m'^2}} \tag{5.8}$$

with $q'^2 = \cos^2 i + q^2 \sin^2 i$, where i is the galaxy inclination.

The observed surface density on the plane of the sky (x, y) is then again given by a sum of 2D Gaussians, with the same σ_j, but different axial ratios q'_j and scaling factors P'_j

$$\Sigma(x, y) = \sum_{j=1}^{N} \frac{q_j \sigma_j \sqrt{2\pi}}{q'_j} P_j \exp\left[-\frac{1}{2\sigma_j^2}\left(x^2 + \frac{y^2}{q_j'^2}\right)\right], \tag{5.9}$$

With the above hypotheses the deprojection is straightforwardly obtained by inverting the above process:

1. one fits an MGE model to an image to determine the P'_j, q'_j and σ_j;
2. one has to assume an inclination i to obtain the $q_j = \sqrt{q_j'^2 - \cos^2 i} \,/ \sin i$ and then the $P_j = P'_j q'_j / (q_j \sigma_j \sqrt{2\pi})$;
3. the intrinsic density is then computed from Equation (5.1).

5.5.2 Integration of a Gaussian on a Grid

In the axisymmetric Schwarzschild modeling we find a linear combination of the orbits that reproduces both the observed kinematics at various apertures and the intrinsic density $\rho(R, z)$ on the meridional plane or, to limit the effect of discretization, also the surface density $\Sigma(x, y)$ on the projected plane. In general the comparison with the density requires a double or triple integration. In the case of an MGE parametrization these computations can be greatly simplified. We discuss below the different cases. We always assume that the Gaussians have a maximum value of one and this means that in the actual computation we have to multiply the results by P'_j, when dealing with meridional plane quantities, and by P_j, when dealing with projected quantities (see previous section).

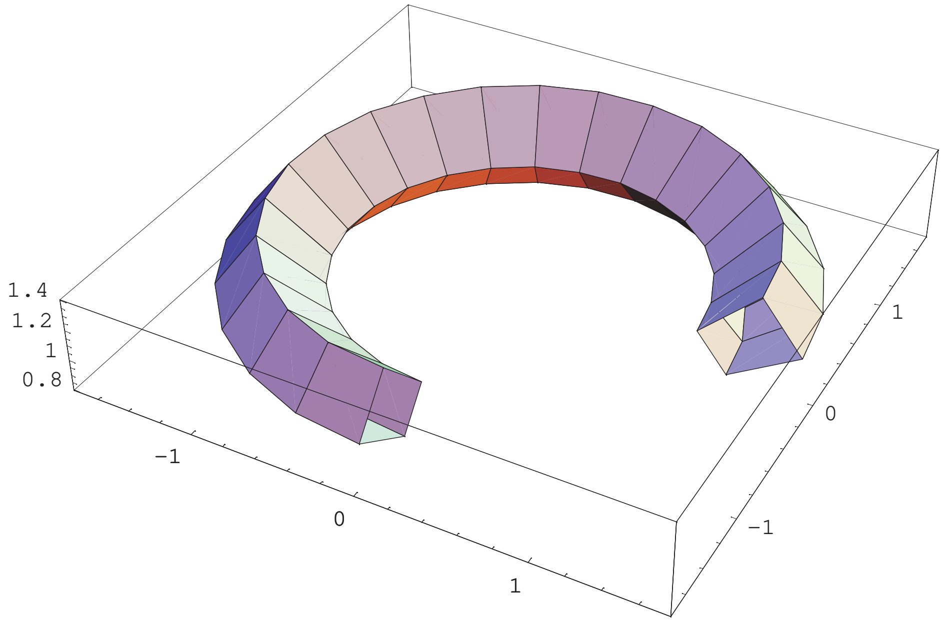

Figure 5.16: One of the elements of the meridional plane grid is shown. Equation 5.11 represents the mass of an axisymmetric Gaussian contained within this region.

Polar grid in the Meridional Plane

We have to integrate an axisymmetric three dimensional Gaussian defined, on the meridional plane, by $\rho(R,z)$ in equation (5.1), on the "torus" D of figure 5.16 around the galaxy symmetry axis, which is delimited by the intervals $[r_0, r_1]$ and $[\theta_0, \theta_1]$ in spherical coordinates ($\theta = 0$ on the symmetry axis). The integrated mass is given in spherical coordinates by

$$\int_D \rho = 2\pi \int_{\theta_0}^{\theta_1} \int_{r_0}^{r_1} e^{-(r/c(\theta))^2}\, r^2 \sin\theta \cdot \mathrm{d}r\, \mathrm{d}\theta \tag{5.10}$$

where $c(\theta) = 2\,q\,\sigma \,/ \sqrt{1+q^2+(1-q^2)\cos 2\theta}$. The inner integration can be performed analytically and the integral becomes

$$\pi \int_{\theta_0}^{\theta_1} \left\{ \frac{\sqrt{\pi}\, c(\theta)}{2} \left[\mathrm{erf}\left(\frac{r_1}{c(\theta)}\right) - \mathrm{erf}\left(\frac{r_0}{c(\theta)}\right) \right] + \right. \\ \left. + r_0\, e^{-(r_0/c(\theta))^2} - r_1\, e^{-(r_1/c(\theta))^2} \right\} c(\theta)^2 \sin\theta \cdot \mathrm{d}\theta \tag{5.11}$$

Polar Grid in the Projected Plane

In the case of the integration of a two dimensional Gaussian on a polar cell D, we have to compute the integral

$$\int_D \Sigma = \int_{\theta_0}^{\theta_1} \int_{r_0}^{r_1} e^{-(r/c(\theta))^2}\, r \cdot \mathrm{d}r\, \mathrm{d}\theta, \tag{5.12}$$

where $\theta = 0$ on the Gaussian minor axis, which gives

$$\int_{\theta_0}^{\theta_1} \frac{c(\theta)^2}{2} \left[e^{-(r_0/c(\theta))^2} - e^{-(r_1/c(\theta))^2} \right] \cdot \mathrm{d}\theta \tag{5.13}$$

Cartesian Grid on the Projected Plane

We compute below the integral of a bidimensional Gaussian on a Cartesian grid D delimited by the intervals $[x_0, x_1]$ and $[y_0, y_1]$. Assuming the grid is parallel to the Gaussian major axis, the integral is given by

$$\int_D \Sigma = \frac{\pi\, q\, \sigma^2}{2} \left[\operatorname{erf}\left(\frac{x_0}{\sqrt{2}\,\sigma}\right) - \operatorname{erf}\left(\frac{x_1}{\sqrt{2}\,\sigma}\right) \right] \left[\operatorname{erf}\left(\frac{y_0}{\sqrt{2}\,q\,\sigma}\right) - \operatorname{erf}\left(\frac{y_1}{\sqrt{2}\,q\,\sigma}\right) \right] \qquad (5.14)$$

If the Gaussian major axis makes an angle θ with the x axis, the double integral on the grid cannot be written explicitly, but can still be expressed as a single integral in one of the coordinates as follows

$$\frac{\sqrt{\pi}\, q\, \sigma}{p} \int_{x_0}^{x_1} \left[\operatorname{erf}\left(\frac{f_0(x)}{2pq\sigma}\right) - \operatorname{erf}\left(\frac{f_1(x)}{2pq\sigma}\right) \right] e^{-[x/(p\,\sigma)]^2} \cdot \mathrm{d}x, \qquad (5.15)$$

with $p = \sqrt{1 + q^2 + (1 - q^2)\cos 2\theta}$ and where we have defined for $k = 0, 1$

$$f_k(x) = (1 - q^2)\, x\, \sin 2\theta - p^2\, y_k \qquad (5.16)$$

5.5.3 Hermite Polynomials

We tabulate below the first six Hermite orthogonal polynomials, following the normalization of van der Marel & Franx (1993). They are written in Horner form for efficient and stable evaluation. The first four are also given in the Appendix of that paper.

$$H_0(y) = 1 \qquad (5.17)$$
$$H_1(y) = \sqrt{2}\, y \qquad (5.18)$$
$$H_2(y) = \frac{-1 + 2\, y^2}{\sqrt{2}} \qquad (5.19)$$
$$H_3(y) = \frac{y\, \left(-3 + 2\, y^2\right)}{\sqrt{3}} \qquad (5.20)$$
$$H_4(y) = \frac{3 + y^2\, \left(-12 + 4\, y^2\right)}{2\,\sqrt{6}} \qquad (5.21)$$
$$H_5(y) = \frac{y\, \left(15 + y^2\, \left(-20 + 4\, y^2\right)\right)}{2\,\sqrt{15}} \qquad (5.22)$$
$$H_6(y) = \frac{-15 + y^2\, \left(90 + y^2\, \left(-60 + 8\, y^2\right)\right)}{12\,\sqrt{5}} \qquad (5.23)$$

These are the polynomials that enter into the computation of the LOSVD as given by equation (5.6).

Bibliography

Binney, J.J., & Tremaine, S.D. 1987, Galactic Dynamics (Princeton: Princeton Univ. Press)

Cardelli, J.A., Clayton, G.C., & Mathis, J.S. 1989, ApJ, 345, 245

Carollo, C.M., Franx, M., Illingworth, G.D., & Forbes, D.A. 1997, ApJ, 481, 710

Chandrasekhar, S. 1969, Ellipsoidals Figures of Equilibrium, (New Haven: Yale University Press)

Cretton, N., & van den Bosch, F. 1999, ApJ, 514, 704

Cretton, N., de Zeeuw, P.T., van der Marel, R.P., & Rix, H. 1999, ApJS, 124, 383

Davies, R.L., Kuntschner, H., Emsellem, E., Bacon, R., Bureau, M., Carollo, C.M., Copin, Y., Miller, B.W., Monnet, G., Peletier, R.F., Verolme, E.K., de Zeeuw, P.T. 2001, ApJ, in press (astro-ph/0011254)

Emsellem, E., Monnet, G., & Bacon, R. 1994, A&A, 285, 723

Favati, P., Lotti, G., & Romani, F. 1991, ACM Transactions On Mathematical Software, Vol. 17, No. 2, pp. 218-232

Faber, S.M., Wegner, G., Burstein, D., Davies, R.L., Dressler, A., Lynden-Bell, D., & Terlevich, R.J. 1989, ApJ, 69, 763

Ferrarese, L., & Merritt, D. 2000, ApJ, 539, L9

Franx, M., & Illingworth, G. D. 1988, ApJ, 327, L55

Franx, M., Illingworth, G.D., & Heckman, T. 1989, AJ, 98, 538

Forbes, D.A., Franx, M., & Illingworth, G. D. 1995, AJ, 109, 1988

Forbes, D.A., & Reitzel, D.B. 1995, AJ, 109, 1576

Gebhardt, K. et al. 2000, ApJ, 539, L13

Malin, D.F. 1985, in New Aspects of Galaxy Photometry, Nieto J.-L., ed, 27 (Berlin: Springer-Verlag)

Monnet, G., Bacon, R., & Emsellem, E. 1992, A&A, 253, 366

Qian, E.E., de Zeeuw, P.T., van der Marel, R.P., & Hunter, C. 1995, MNRAS, 274, 602

Rix, H.-W., de Zeeuw, P.T., Cretton N., van der Marel, R.P., & Carollo, C.M. 1997, ApJ, 488, 702

Rybicki, G. B. 1986, in Structure and Dynamics of Elliptical Galaxies, ed. P.T. de Zeeuw (Dordrecht: Reidel), 397

Schwarzschild, M. 1979, ApJ, 232, 236

Scorza, C., & van den Bosch, F.C. 1998, MNRAS, 300, 469

Tonry, J.L. et al. 2000, ApJS, in press (astro-ph/0011223)

van der Marel, R.P., & Franx, M. 1993, ApJ, 407, 525

van der Marel, R.P., Cretton, N., de Zeeuw, P.T., & Rix, H. 1998, ApJ, 493, 613

Verdoes Kleijn, G.A., van der Marel, R.P., Carollo, C.M., & de Zeeuw, P.T. 2000, AJ, 120, 1221